Title

Decoupling Carrier Dynamics and Energy Transport in Ultrafast Near-Field Nanoscopy.

Permalink

https://escholarship.org/uc/item/2h25q55d

Journal

Nano Letters, 25(6)

Authors

Yang, Rundi

Li, Runxuan

Blankenship, Brian

et al.

Publication Date

2025-02-12

DOI

10.1021/acs.nanolett.4c05419

Peer reviewed

Decoupling Carrier Dynamics and Energy Transport in Ultrafast Near-Field Nanoscopy

Rundi Yang,[#] Runxuan Li,[#] Brian W. Blankenship, Jingang Li,* and Costas P. Grigoropoulos*
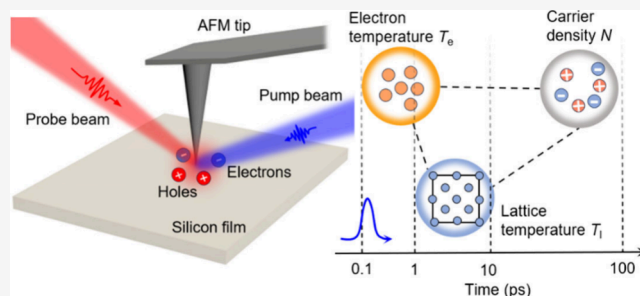
ACCESS | Metrics & More | Article Recommendations | SI Supporting Information

ABSTRACT: Ultrafast near-field optical nanoscopy has emerged as a powerful platform to characterize low-dimensional materials. While analytical and numerical models have been established to account for photoexcited carrier dynamics, quantitative evaluation of the associated pulsed laser heating remains elusive. Here, we decouple the photocarrier density and temperature increase in near-field nanoscopy by integrating the two-temperature model (TTM) with finite-difference time-domain (FDTD) simulations. These results reveal that the electron−phonon coupling in a silicon film after femtosecond laser excitation is most pronounced within approximately 3 ps—substantially shorter than the photocarrier decay time scale at tens of picoseconds. Moreover, the coupled TTM-FDTD method indicates that ultrafast laser heating can cause up to a 14% variation in the near-field signal at a 220 μJ/cm^2 pump pulse fluence. Our numerical results are further validated by transient experiments, highlighting the potential of this method for investigations of carrier and thermal phenomena in emerging nanomaterials and nanodevices.

KEYWORDS: *pump−probe, s-SNOM, carrier dynamics, ultrafast laser heating, two-temperature model, FDTD*

The rapid development of nanoscience and nanotechnology has called for new tools for the characterization of low-dimensional materials with nanometer spatial resolutions. Recently, tip-based optical microscopy techniques, particularly scattering-type scanning near-field optical microscopy (s-SNOM), have been developed as versatile platforms to probe various nanoscale materials.[1] With a subdiffraction-limit spatial resolution, s-SNOM is capable of imaging the locally inhomogeneous photonics modes and states in dielectric[2,3] and plasmonic[4,5] nanostructures. Moreover, many novel physical phenomena in emerging quantum materials have been unveiled by s-SNOM, including phase transitions,[6,7] polariton propagation,[8−10] and optical waveguiding.[11−13]

While s-SNOM has been primarily employed to resolve static materials properties, the recent integration with pump−probe optics has extended its capability to investigate ultrafast dynamic material responses.[14,15] With high resolutions in both space and time domains, pump−probe s-SNOM is a promising tool for the exploration of transient transport phenomena at the nanoscale, including the nonequilibrium characteristics of plasmons, phonons, and exciton−polaritons in various semi-metallic and semiconducting materials.[15−19] Additionally, transient near-field measurements have been reported to effectively reveal nanoscale carrier dynamics and transport in semiconductor materials and heterostructures.[14,20−23]

The quantitative analysis of pump−probe s-SNOM is based on the light-induced refractive index change that is described by the Drude model. This effect is usually attributed solely to

the photoexcited carrier density.[15,20,24] Consequently, the effects of lattice heating and the associated electron−phonon interactions are not thoroughly considered.[25] While near-field nanothermometry has been demonstrated to measure the steady-state temperatures of hot electrons and Joule-heated lattices in microelectronic devices,[26−29] the analysis of complex coupling between electrons and the lattice in transient near-field nanoscopy remains challenging. Nevertheless, a full understanding of the transient carrier behaviors and lattice heating is crucial for controlling excessive heat generation in fast switching optoelectronic devices, an issue that may diminish device efficiency and performance.[25,30] In addition, these insights will also facilitate the fundamental study of nanoscale thermal transport in semiconductor materials.[31,32]
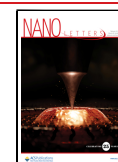
In this work, we untangle the convoluted carrier dynamics and energy transport in pump−probe s-SNOM. Taking silicon as an example, we numerically solve the spatiotemporal electron temperature, lattice temperature, and carrier density upon pulsed laser excitation by coupling the two-temperature model (TTM) with finite-difference time-domain (FDTD)
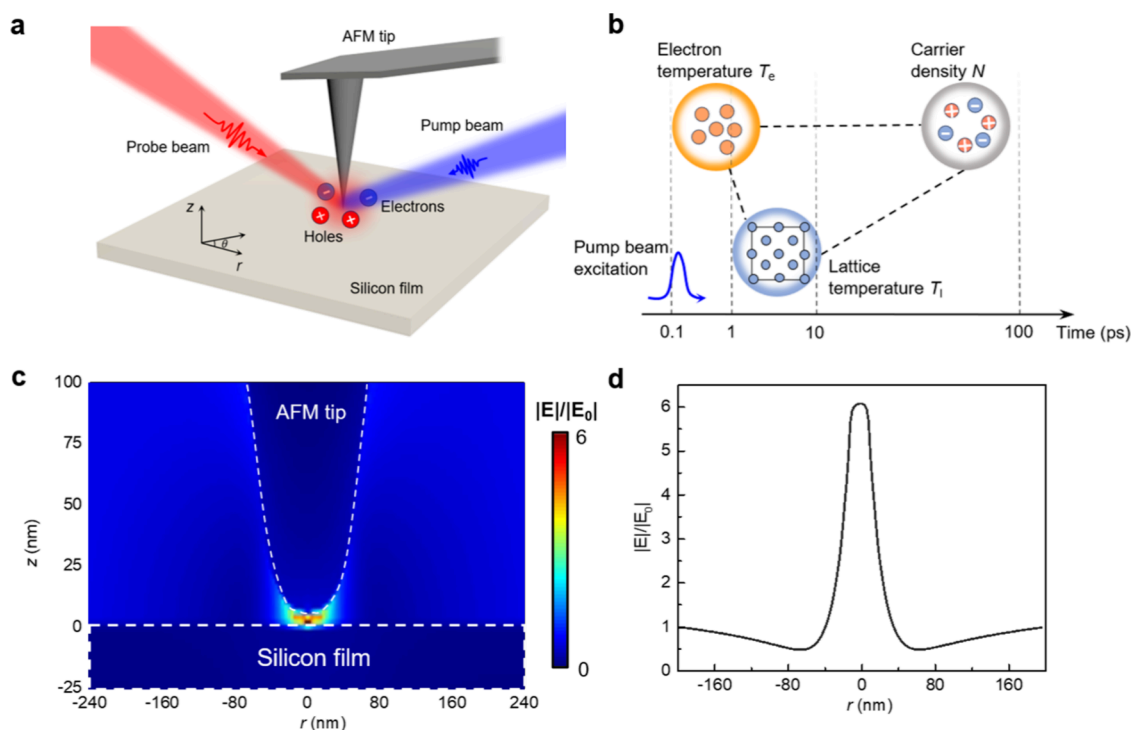
Figure 1. (a) The schematic of the pump−probe s-SNOM setup. (b) The time scale of the electron temperature, lattice temperature, and carrier density and the coupling among them. (c) The FDTD simulated electric field distribution at the cross-section of the tip−sample interface under pump beam illumination. (d) The electric field enhancement profile as a function of the radial distance on the silicon surface.

simulations. Silicon is chosen as the test material because of the availability of fundamental transport properties, including from reported far-field pump−probe experiments. It is demonstrated that upon near-infrared probe beam irradiation, lattice heating contributes to the near-field signal, leading to a difference of ~14% at a high pump fluence of 220 μJ/cm². Transient measurements are also performed on a silicon wafer, where the time-resolved s-SNOM signals are well predicted by the developed TTM-FDTD model. Our results present a versatile framework for the investigation of ultrafast carrier dynamics and energy transport in semiconductor materials.

The setup of our pump−probe s-SNOM is shown in Figure 1a. A visible pump beam (400 nm) and a near-infrared probe beam (800 nm) are directed to an atomic force microscope (AFM) tip with a controlled time delay (see Note S1 for more details). Upon pump beam illumination, the silicon substrate target primarily undergoes three processes: photoexcitation of electrons and holes, temperature rise of electrons driven by the laser energy absorption, and lattice heating due to electron−phonon coupling. These processes can be quantified by considering the time-dependent carrier density N, electron temperature T_e, and lattice temperature T_l, respectively, which evolve in different time scales (Figure 1b).[33] The two-temperature model (TTM) below is utilized to describe the laser−matter interaction:[33−35]

$$\frac{\partial N}{\partial t} = \nabla(D\nabla N) + \frac{\alpha(1-R)I}{h\nu} + \frac{\beta(1-R)^2I^2}{2h\nu} - \gamma N^3$$

(1)

$$C_e\frac{\partial T_e}{\partial t} = \nabla(k_e\nabla T_e) - G(T_e - T_l) + \frac{\alpha(1-R)I}{h\nu}(h\nu - E_g)$$
$$+ \frac{\beta(1-R)^2I^2}{h\nu}(2h\nu - E_g)$$

(2)

$$C_l\frac{\partial T_l}{\partial t} = \nabla(k_l\nabla T_l) + G(T_e - T_l)$$

(3)

where I is the local pump beam intensity in the irradiated target; α and β are the single-photon and two-photon absorption coefficients, respectively; $h\nu$ is the pump beam photon energy; γ is the Auger recombination rate; $C_e(C_l)$ and $k_e(k_l)$ are the heat capacitance and thermal conductivity of electrons (lattice); G is the electron−phonon coupling coefficient; R is the surface reflectivity; and E_g is the bandgap of silicon (see Table S2 in Note S2 for parameters).[33,36−41] Equations 1−3 are coupled as the dielectric permittivity and the optical properties depend on the spatially and temporally varying carrier density and temperature (Note S2, Equations S4−S8).

Here we consider the TTM in the two-dimensional (2D) case, where the quantities vary in the radial (r) and vertical (z) directions (Note S3). The incoming femtosecond laser pump light generates a concentrated spot on the target substrate surface underneath the tip that is fitted to a Gaussian spatiotemporal intensity distribution:[34]

$$I(r, z = 0, t) = 0.94I_{tip} \exp\left(-2.77\left(\frac{t-t_0}{t_p}\right)^2 - \frac{2r^2}{r_0^2}\right)$$

(4)

where $I_{tip} = I_0(E^2/E_0^2)$ is the estimated peak laser intensity underneath the tip; $I_0 = F_0/t_p$ is the incoming peak laser
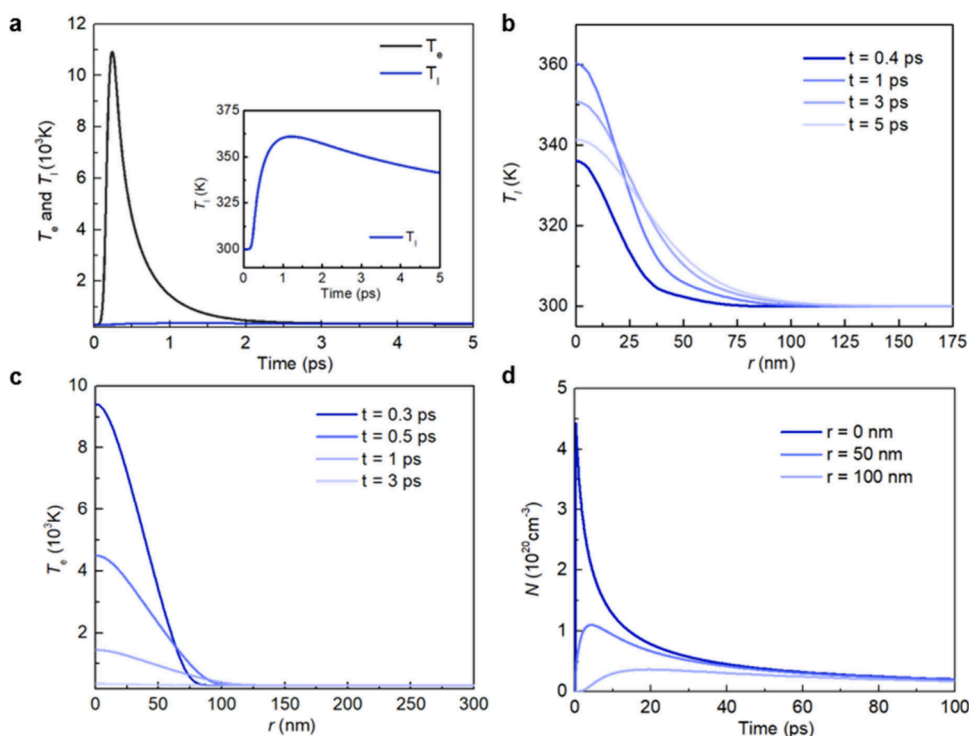
Figure 2. Finite-difference simulation of TTM with a laser fluence of F_0 = 125 μJ/cm^2. (a) Time-resolved electron and lattice temperatures of the silicon surface at the pump laser beam center. Inset: the transient profile of the lattice temperature. (b, c) Radial distribution of the (b) lattice temperature and (c) electron temperature at different times (z = 0 nm). (d) Time-resolved carrier density at different radial locations on the silicon surface (z = 0 nm).
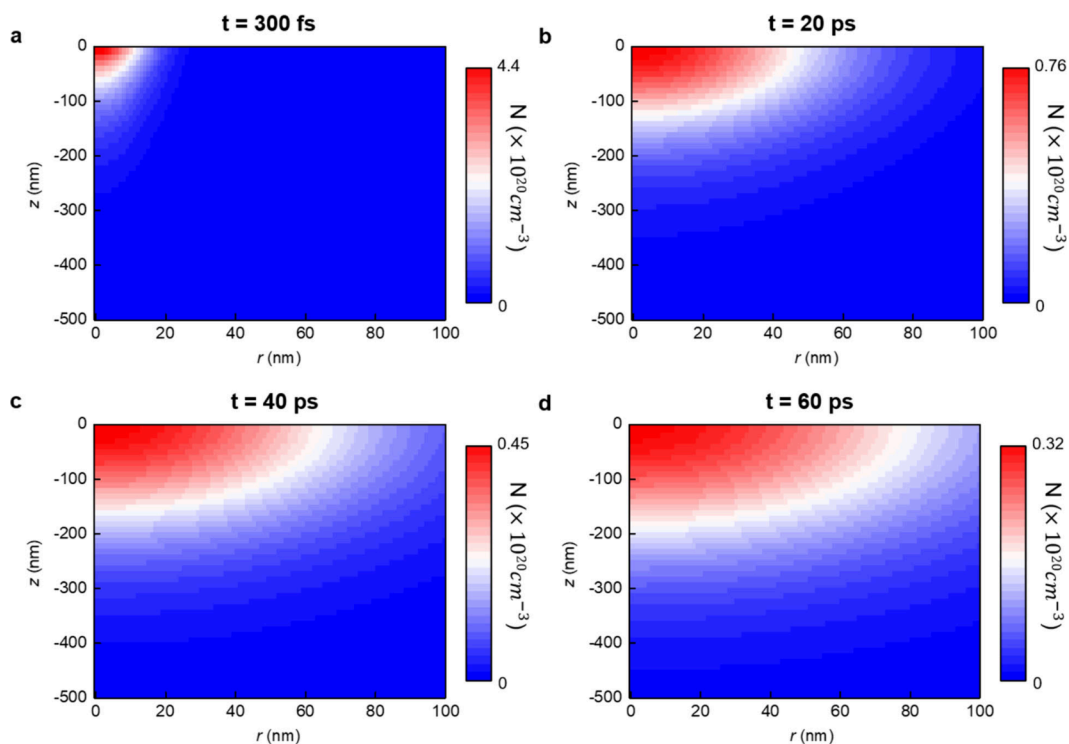

Figure 3. Spatial distribution of the carrier density at (a) t = 300 fs, (b) t = 20 ps, (c) t = 40 ps, and (d) t = 60 ps. The distribution of carriers expands spatially over time.

intensity; F_0 is the incoming laser fluence; E^2/E_0^2 is the electric field enhancement; t_p = 83 fs is the half-peak pulse width; t is the time; t_0 = 200 fs is the pulse peak time; and r is the radial location. r_0 corresponds to the spot radius determined from the

FDTD simulations (see Note S4 for more details).[42,43] Figure 1c shows the simulated electric field distribution at the cross-section of the s-SNOM system at a tip−sample distance of 4 nm, where a clear near-field enhancement at the tip−sample
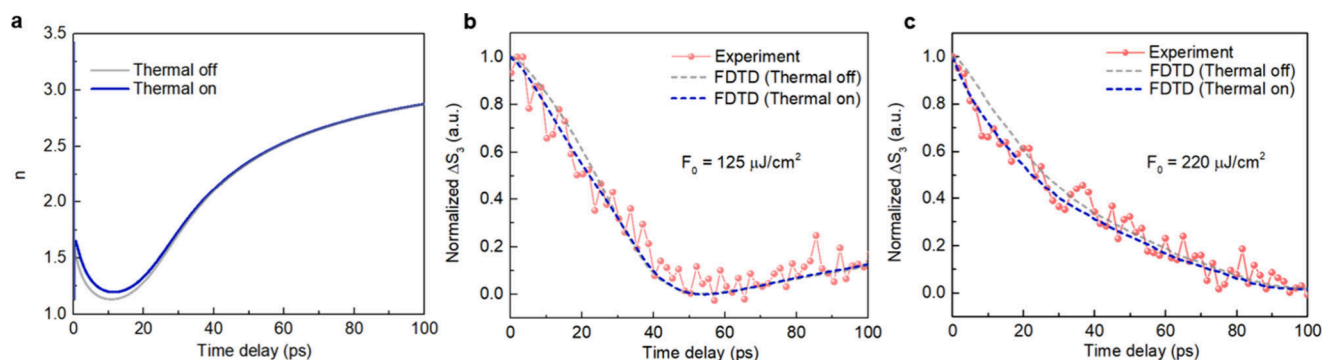
Figure 4. (a) Time-resolved refractive index n of silicon when the lattice heating is considered (thermal on) and when the lattice temperature is kept at 300 K (thermal off). (b, c) The transient s-SNOM measurements and simulated near-field signals at the fluence of (b) 125 μJ/cm^2 and (c) 220 μJ/cm^2.

interface can be observed. By extracting the profile of the electric field on the silicon surface (in the r direction), we estimate the $1/e^2$ spot radius r_0 of the laser beam to be ~40 nm (Figure 1d). In the z direction, the optical intensity decreases as silicon absorbs the laser energy, which can be modeled by (Figure S2 and Note S2):[34]

$$\frac{\partial I(t, z, r)}{\partial z} = -\alpha I(t, z, r) - \beta I(t, z, r)^2 \qquad (5)$$

The numerical simulation of TTM is conducted by utilizing the finite-difference algorithm (see Note S3 for more details). Based on our experimental setup, a typical incoming laser fluence $F_0 = 125$ μJ/cm^2 results in a peak intensity of ~51 GW/cm^2 at the film surface underneath the tip (Figure S3). The simulation results show that the energy exchange between the electron and lattice primarily occurs in the first ~3 ps (Figure 2a). Notably, the lattice temperature (T_l) starts to decrease before this time (inset of Figure 2a), as the difference between T_e and T_l is sufficiently small to make thermal diffusion prevail over the electron−phonon coupling after ~1.2 ps. In other words, on the right side of eq 3, the first term dwarfs the second. This diffusion effect can also be visualized from the flattening in spatial profiles of both T_l (Figures 2b, S4, and S5) and T_e (Figures 2c, and S4, and S5) with time. Compared to the temperature profiles, the temporal evolution of carrier density occurs at a much longer time scale with a clear spatial dependence (Figure 2d). This phenomenon exhibits competition among photocarrier injection, carrier diffusion, and Auger recombination (eq 1), which can be further manifested by mapping the carrier distribution at several critical times (Figure 3). At early times, carriers are concentrated in a small region at the silicon surface (Figure 3a), which is primarily determined by the spot radius and penetration depth of the pump beam radiation that is focused underneath the tip. As time increases, the carrier distribution expands both radially and vertically (Figure 3b to 3d) due to the carrier diffusion driven by the density gradient. In addition, carrier recombination leads to a temporal decay in the overall magnitude of the carrier population (Figure 3).

The spatiotemporal carrier density and lattice temperature after pump beam excitation both affect the transient optical response of the irradiated silicon and the resultant s-SNOM signal. The near-field probe light distribution depends on the varying refractive index n and extinction coefficient k of the affected domain at the respective wavelength, which can be calculated from the Drude model (Figure 4a and Note S5). To

weigh the influence of the carrier density versus the lattice temperature, we also calculate n and k by using a constant lattice temperature of 300 K in Equation S8 (Figures 4a and S6). While the effect of carrier population dominates the optical coefficients, lattice heating can lead to a difference of ~8% in n and less than 1% in k. We subsequently use FDTD simulations to calculate the time-resolved s-SNOM signal ΔS_3 (Note S6).[44] Recently, advanced analytical models have been developed to consider the out-of-plane carrier profile;[45] here, we directly model the spatially resolved optical coefficients in FDTD simulations, which takes into account both the in-plane and out-of-plane carrier/temperature profiles.

Last, we perform near-field transient measurements on a silicon wafer to verify the simulation results. The normalized time-resolved s-SNOM signal obtained from the experiment shown in Figure 4b matches the simulation well. Similarly, ΔS_3 is jointly influenced by the carrier density and the lattice temperature. To evaluate their respective contributions, we also simulate the s-SNOM intensity while keeping the temperature of the silicon substrate uniform at 300 K. The comparison of both cases indicates that laser heating can lead to a maximum difference in ΔS_3 of ~9% (Figure 4b), which primarily appears in the first 30 ps when the lattice temperature is relatively high (Figure S8). To further validate the developed TTM-FDTD method, we carried out transient measurements and numerical simulations at a higher fluence of $F_0 = 220$ μJ/cm^2 (Figure 4c). In this case, lattice heating produces a larger difference of up to ~14% in ΔS_3, owing to a higher lattice temperature at elevated laser fluence (Figure S9). These results necessitate the consideration of lattice temperature variation in systems with relatively high fluence and temperature change, such as the laser processing of nanomaterials[46] and thermoelectric materials.[32] This study therefore provides a methodology to characterize and decouple the carrier and energy transport behaviors in these systems.

In summary, we demonstrate a comprehensive analysis of carrier dynamics and energy transport in ultrafast near-field nanoscopy. The finite-difference numerical simulation of TTM reveals much longer dynamics of photoexcited carriers compared to the electron−phonon coupling that occurs within a timespan of ~3 ps pursuant to the ultrafast pump laser excitation. By coupling the TTM and FDTD simulations, we show that while carrier density dominates the near-field response, the lattice heating can lead to a considerable contribution to the s-SNOM signal that increases as higher laser fluences are applied. The numerical solutions are also

verified by pump−probe s-SNOM experiments. While crystalline silicon film is used as the example material in this study, this coupled TTM-FDTD method is generally applicable to a wide range of emerging materials and nanostructures, including III−V semiconductors,[14,47] low-dimensional materials,[48−50] and perovskites.[45] Additionally, this method can be applied for interrogating carrier behaviors and energy transport in functional electrothermal and photothermal devices.[51−53]

■ ASSOCIATED CONTENT

Ⓢ Supporting Information

The Supporting Information is available free of charge at https://pubs.acs.org/doi/10.1021/acs.nanolett.4c05419.

> Supporting Notes 1−6 on experimental and simulation methods; Supporting Tables 1−2 on parameters used in TTM and Drude model; and Supporting Figures 1−9 on additional data and analysis (PDF)

■ AUTHOR INFORMATION

Corresponding Authors

Costas P. Grigoropoulos − *Laser Thermal Laboratory, Department of Mechanical Engineering, University of California, Berkeley, California 94720, United States;* ⓞ orcid.org/0000-0002-8505-4037; Email: cgrigoro@berkeley.edu

Jingang Li − *Laser Thermal Laboratory, Department of Mechanical Engineering, University of California, Berkeley, California 94720, United States;* ⓞ orcid.org/0000-0003-0827-9758; Email: jingang@berkeley.edu

Authors

Rundi Yang − *Laser Thermal Laboratory, Department of Mechanical Engineering, University of California, Berkeley, California 94720, United States;* ⓞ orcid.org/0000-0002-2877-939X

Runxuan Li − *Laser Thermal Laboratory, Department of Mechanical Engineering, University of California, Berkeley, California 94720, United States*

Brian W. Blankenship − *Laser Thermal Laboratory, Department of Mechanical Engineering, University of California, Berkeley, California 94720, United States;* ⓞ orcid.org/0000-0003-4212-6835

Complete contact information is available at:
https://pubs.acs.org/10.1021/acs.nanolett.4c05419

Author Contributions

#R.Y. and R.L. contributed equally to this work.

Notes

The authors declare no competing financial interest.

■ ACKNOWLEDGMENTS

■ REFERENCES

(1) Chen, X.; Hu, D.; Mescall, R.; You, G.; Basov, D. N.; Dai, Q.; Liu, M. Modern Scattering-Type Scanning Near-Field Optical Microscopy for Advanced Material Research. *Adv. Mater.* **2019**, *31*, 1804774.

(2) Mastel, S.; Govyadinov, A. A.; Maissen, C.; Chuvilin, A.; Berger, A.; Hillenbrand, R. Understanding the Image Contrast of Material Boundaries in IR Nanoscopy Reaching 5 nm Spatial Resolution. *ACS Photonics* **2018**, *5*, 3372−3378.

(3) Vakulenko, A.; Kiriushechkina, S.; Wang, M.; Li, M.; Zhirihin, D.; Ni, X.; Guddala, S.; Korobkin, D.; Alù, A.; Khanikaev, A. B. Near-Field Characterization of Higher-Order Topological Photonic States at Optical Frequencies. *Adv. Mater.* **2021**, *33*, 2004376.

(4) Fei, Z.; Andreev, G. O.; Bao, W.; Zhang, L. M.; Mcleod, A. S.; Wang, C.; Stewart, M. K.; Zhao, Z.; Dominguez, G.; Thiemens, M.; et al. Infrared Nanoscopy of Dirac Plasmons at the Graphene-SiO₂ Interface. *Nano Lett.* **2011**, *11*, 4701−4705.

(5) Hu, F.; Luan, Y.; Fei, Z.; Palubski, I. Z.; Goldflam, M. D.; Dai, S.; Wu, J.-S.; Post, K. W.; Janssen, G. C. A. M.; Fogler, M. M.; et al. Imaging the Localized Plasmon Resonance Modes in Graphene Nanoribbons. *Nano Lett.* **2017**, *17*, 5423−5428.

(6) Yang, R.; Li, J.; Cai, Y.; Blankenship, B. W.; Wu, J.; Grigoropoulos, C. P. Near-Field Nanoimaging of Phases and Carrier Dynamics in Vanadium Dioxide Nanobeams. *ACS Photonics* **2024**, *11*, 3359−3364.

(7) Huber, M. A.; Plankl, M.; Eisele, M.; Marvel, R. E.; Sandner, F.; Korn, T.; Schüller, C.; Haglund, R. F.; Huber, R.; Cocker, T. L. Ultrafast Mid-Infrared Nanoscopy of Strained Vanadium Dioxide Nanobeams. *Nano Lett.* **2016**, *16*, 1421−1427.

(8) Dai, S.; Fei, Z.; Ma, Q.; Rodin, A. S.; Wagner, M.; McLeod, A. S.; Liu, M. K.; Gannett, W.; Regan, W.; Watanabe, K.; et al. Tunable Phonon Polaritons in Atomically Thin van der Waals Crystals of Boron Nitride. *Science* **2014**, *343*, 1125−1129.

(9) Hu, F.; Luan, Y.; Scott, M. E.; Yan, J.; Mandrus, D. G.; Xu, X.; Fei, Z. Imaging exciton-polariton transport in MoSe2 waveguides. *Nat. Photonics* **2017**, *11*, 356−360.

(10) Basov, D. N.; Fogler, M. M.; Garcia de Abajo, F. J. Polaritons in van der Waals materials. *Science* **2016**, *354*, 1992.

(11) Liu, Y.; Li, J.; Zhu, Y.; Ai, Q.; Xu, R.; Yang, R.; Zhang, B.; Fang, Q.; Zhai, T.; Xu, C.; et al. Spatially Resolved Anion Diffusion and Tunable Waveguides in Bismuth Halide Perovskites. *Nano Lett.* **2024**, *24*, 5182−5188.

(12) Li, J.; Yang, R.; Yao, K.; Huang, Y.; Rho, Y.; Fan, D. E.; Zheng, Y.; Grigoropoulos, C. P. Near-Field Nanoimaging of Colloidal Transition Metal Dichalcogenide Waveguides. *Adv. Funct. Mater.* **2024**, *34*, 2312127.

(13) Ling, H.; Manna, A.; Shen, J.; Tung, H.-T.; Sharp, D.; Fröch, J.; Dai, S.; Majumdar, A.; Davoyan, A. R. Deeply subwavelength integrated excitonic van der Waals nanophotonics. *Optica* **2023**, *10*, 1345−1352.

(14) Eisele, M.; Cocker, T. L.; Huber, M. A.; Plankl, M.; Viti, L.; Ercolani, D.; Sorba, L.; Vitiello, M. S.; Huber, R. Ultrafast multi-terahertz nano-spectroscopy with sub-cycle temporal resolution. *Nat. Photonics* **2014**, *8*, 841−845.

(15) Wagner, M.; Fei, Z.; McLeod, A. S.; Rodin, A. S.; Bao, W.; Iwinski, E. G.; Zhao, Z.; Goldflam, M.; Liu, M.; Dominguez, G.; et al. Ultrafast and Nanoscale Plasmonic Phenomena in Exfoliated Graphene Revealed by Infrared Pump-Probe Nanoscopy. *Nano Lett.* **2014**, *14*, 894−900.

(16) Charnukha, A.; Sternbach, A.; Stinson, H. T.; Schlereth, R.; Brüne, C.; Molenkamp, L. W.; Basov, D. N. Ultrafast nonlocal collective dynamics of Kane plasmon-polaritons in a narrow-gap semiconductor. *Sci. Adv.* **2019**, *5*, No. eaau9956.

(17) Gilburd, L.; Xu, X. G.; Bando, Y.; Golberg, D.; Walker, G. C. Near-Field Infrared Pump-Probe Imaging of Surface Phonon Coupling in Boron Nitride Nanotubes. *J. Phys. Chem. Lett.* **2016**, *7*, 289−294.

(18) Mrejen, M.; Yadgarov, L.; Levanon, A.; Suchowski, H. Transient exciton-polariton dynamics in WSe₂ by ultrafast near-field imaging. *Sci. Adv.* **2019**, *5*, No. eaat9618.

(19) Yao, Z.; Xu, S.; Hu, D.; Chen, X.; Dai, Q.; Liu, M. Nanoimaging and Nanospectroscopy of Polaritons with Time Resolved s-SNOM. *Adv. Optical Mater.* **2020**, *8*, 1901042.

(20) Li, J.; Yang, R.; Rho, Y.; Ci, P.; Eliceiri, M.; Park, H. K.; Wu, J.; Grigoropoulos, C. P. Ultrafast Optical Nanoscopy of Carrier Dynamics in Silicon Nanowires. *Nano Lett.* **2023**, *23*, 1445−1450.

(21) Plankl, M.; Faria Junior, P. E.; Mooshammer, F.; Siday, T.; Zizlsperger, M.; Sandner, F.; Schiegl, F.; Maier, S.; Huber, M. A.; Gmitra, M.; et al. Subcycle contact-free nanoscopy of ultrafast interlayer transport in atomically thin heterostructures. *Nat. Photonics* **2021**, *15*, 594−600.

(22) Merkl, P.; Mooshammer, F.; Steinleitner, P.; Girnghuber, A.; Lin, K. Q.; Nagler, P.; Holler, J.; Schüller, C.; Lupton, J. M.; Korn, T.; et al. Ultrafast transition between exciton phases in van der Waals heterostructures. *Nat. Mater.* **2019**, *18*, 691−696.

(23) Li, J.; Yang, R.; Higashitarumizu, N.; Dai, S.; Wu, J.; Javey, A.; Grigoropoulos, C. P. Transient Nanoscopy of Exciton Dynamics in 2D Transition Metal Dichalcogenides. *Adv. Mater.* **2024**, *36*, 2311568.

(24) Huber, A. J.; Kazantsev, D.; Keilmann, F.; Wittborn, J.; Hillenbrand, R. Simultaneous IR Material Recognition and Conductivity Mapping by Nanoscale Near-Field Microscopy. *Adv. Mater.* **2007**, *19*, 2209−2212.

(25) Weaver, H. L.; Went, C. M.; Wong, J.; Jasrasaria, D.; Rabani, E.; Atwater, H. A.; Ginsberg, N. S. Detecting, Distinguishing, and Spatiotemporally Tracking Photogenerated Charge and Heat at the Nanoscale. *ACS Nano* **2023**, *17*, 19011−19021.

(26) Weng, Q.; Komiyama, S.; Yang, L.; An, Z.; Chen, P.; Biehs, S.-A.; Kajihara, Y.; Lu, W. Imaging of nonlocal hot-electron energy dissipation via shot noise. *Science* **2018**, *360*, 775−778.

(27) Gramse, G.; Kölker, A.; Škereň, T.; Stock, T. J. Z.; Aeppli, G.; Kienberger, F.; Fuhrer, A.; Curson, N. J. Nanoscale imaging of mobile carriers and trapped charges in delta doped silicon p−n junctions. *Nature Electronics* **2020**, *3*, 531−538.

(28) Menges, F.; Mensch, P.; Schmid, H.; Riel, H.; Stemmer, A.; Gotsmann, B. Temperature mapping of operating nanoscale devices by scanning probe thermometry. *Nat. Commun.* **2016**, *7*, 10874.

(29) Weng, Q.; Lin, K.-T.; Yoshida, K.; Nema, H.; Komiyama, S.; Kim, S.; Hirakawa, K.; Kajihara, Y. Near-Field Radiative Nanothermal Imaging of Nonuniform Joule Heating in Narrow Metal Wires. *Nano Lett.* **2018**, *18*, 4220−4225.

(30) Waldrop, M. M. The chips are down for Moore's law. *Nature* **2016**, *530*, 144−147.

(31) Weng, Q.; Yang, L.; An, Z.; Chen, P.; Tzalenchuk, A.; Lu, W.; Komiyama, S. Quasiadiabatic electron transport in room temperature nanoelectronic devices induced by hot-phonon bottleneck. *Nat. Commun.* **2021**, *12*, 4752.

(32) Yu, Y.; Xu, X.; Wang, Y.; Jia, B.; Huang, S.; Qiang, X.; Zhu, B.; Lin, P.; Jiang, B.; Liu, S.; et al. Tunable quantum gaps to decouple carrier and phonon transport leading to high-performance thermoelectrics. *Nat. Commun.* **2022**, *13*, 5612.

(33) Liu, J.; Wu, M.; Sun, Z.; Zhang, Q.; Zhu, Y.; Fu, Y. The picosecond laser ablation mechanism of monocrystalline silicon by coupling two-temperature model (TTM)-Molecular dynamic (MD). *Appl. Surf. Sci.* **2024**, *661*, 160022.

(34) Tsibidis, G. D.; Stratakis, E.; Aifantis, K. E. Thermoplastic deformation of silicon surfaces induced by ultrashort pulsed lasers in submelting conditions. *J. Appl. Phys.* **2012**, *111*, 053502.

(35) Segovia, M.; Xu, X. Ultrafast, high resolution spatiotemporal mapping of energy transport dynamics for determination of energy transport properties in silicon. *Phys. Rev. B* **2023**, *108*, 125202.

(36) Mouskeftaras, A.; Chanal, M.; Chambonneau, M.; Clady, R.; Utéza, O.; Grojo, D. Direct measurement of ambipolar diffusion in bulk silicon by ultrafast infrared imaging of laser-induced microplasmas. *Appl. Phys. Lett.* **2016**, *108*, 041107.

(37) van Driel, H. M. Kinetics of high-density plasmas generated in Si by 1.06- and 0.53-μm picosecond laser pulses. *Phys. Rev. B* **1987**, *35*, 8166−8176.

(38) Chen, J. K.; Tzou, D. Y.; Beraun, J. E. Numerical investigation of ultrashort laser damage in semiconductors. *Int. J. Heat Mass Transfer* **2005**, *48*, 501−509.

(39) Tsibidis, G. D.; Barberoglou, M.; Loukakos, P. A.; Stratakis, E.; Fotakis, C. Dynamics of ripple formation on silicon surfaces by ultrashort laser pulses in subablation conditions. *Phys. Rev. B* **2012**, *86*, 115346.

(40) Sproul, A. B.; Green, M. A. Improved value for the silicon intrinsic carrier concentration from 275 to 375 K. *J. Appl. Phys.* **1991**, *70*, 846−854.

(41) Agassi, D. Phenomenological model for pisosecond-pulse laser annealing of semiconductors. *J. Appl. Phys.* **1984**, *55*, 4376−4383.

(42) Chimmalgi, A.; Grigoropoulos, C. P.; Komvopoulos, K. Surface nanostructuring by nano-/femtosecond laser-assisted scanning force microscopy. *J. Appl. Phys.* **2005**, *97*, 104319.

(43) Meng, L.; Yang, Z.; Chen, J.; Sun, M. Effect of Electric Field Gradient on Sub-nanometer Spatial Resolution of Tip-enhanced Raman Spectroscopy. *Sci. Rep.* **2015**, *5*, 9240.

(44) Yang, R.; Li, J.; Grigoropoulos, C. P. Numerical Study of Carrier Dynamics in Pump-Probe Near-Field Nanoscopy. *J. Phys. Chem. C* **2024**, *128*, 261−267.

(45) Zizlsperger, M.; Nerreter, S.; Yuan, Q.; Lohmann, K. B.; Sandner, F.; Schiegl, F.; Meineke, C.; Gerasimenko, Y. A.; Herz, L. M.; Siday, T.; et al. In situ nanoscopy of single-grain nanomorphology and ultrafast carrier dynamics in metal halide perovskites. *Nat. Photonics* **2024**, *18*, 975−981.

(46) Li, R.; Blankenship, B. W.; Wu, J.; Rho, Y.; Li, J.; Grigoropoulos, C. P. Laser-aided processing and functionalization of 2D materials. *Appl. Phys. Lett.* **2024**, *125*, 070502.

(47) Del Alamo, J. A. Nanometre-scale electronics with III-V compound semiconductors. *Nature* **2011**, *479*, 317−323.

(48) Boukai, A. I.; Bunimovich, Y.; Tahir-Kheli, J.; Yu, J.-K.; Goddard, W. A., Iii; Heath, J. R. Silicon nanowires as efficient thermoelectric materials. *Nature* **2008**, *451*, 168−171.

(49) Meineke, C.; Schlosser, J.; Zizlsperger, M.; Liebich, M.; Nilforoushan, N.; Mosina, K.; Terres, S.; Chernikov, A.; Sofer, Z.; Huber, M. A.; et al. Ultrafast Exciton Dynamics in the Atomically Thin van der Waals Magnet CrSBr. *Nano Lett.* **2024**, *24*, 4101−4107.

(50) Li, J.; Zheng, Y. Optothermally Assembled Nanostructures. *Acc. Mater. Res.* **2021**, *2*, 352−363.

(51) Sui, D.; Huang, Y.; Huang, L.; Liang, J.; Ma, Y.; Chen, Y. Flexible and Transparent Electrothermal Film Heaters Based on Graphene Materials. *Small* **2011**, *7*, 3186−3192.

(52) Blankenship, B. W.; Li, R.; Guo, R.; Zhao, N.; Shin, J.; Yang, R.; Ko, S. H.; Wu, J.; Rho, Y.; Grigoropoulos, C. Photothermally Activated Artificial Neuromorphic Synapses. *Nano Lett.* **2023**, *23*, 9020−9025.

(53) Gabor, N. M.; Song, J. C. W.; Ma, Q.; Nair, N. L.; Taychatanapat, T.; Watanabe, K.; Taniguchi, T.; Levitov, L. S.; Jarillo-Herrero, P. Hot Carrier-Assisted Intrinsic Photoresponse in Graphene. *Science* **2011**, *334*, 648−652.